This article has been accepted for inclusion in a future issue of this journal. Content is final as presented, with the exception of pagination.

Instrument Design and Performance of the High-Frequency Airborne Microwave and Millimeter-Wave Radiometer

Xavier Bosch-Lluis, *Senior Member, IEEE*, Steven C. Reising, *Senior Member, IEEE*, Pekka Kangaslahti, *Member, IEEE*, Alan B. Tanner, Shannon T. Brown, Sharmila Padmanabhan, Chaitali Parashare, Oliver Montes, Behzad Razavi, Victoria D. Hadel, Thaddeus P. Johnson, Mehmet Ogut, and James Ranson

***Abstract*—The high-frequency airborne microwave and millimeter-wave radiometer (HAMMR) is a cross-track scanning airborne radiometer instrument with 25 channels from 18.7 to 183.3 GHz. HAMMR includes: low-frequency microwave channels at 18.7, 23.8, and 34.0 GHz at two linear-orthogonal polarizations; high-frequency millimeter-wave channels at 90, 130 and 168 GHz; and millimeter-wave sounding channels consisting of eight channels near the 118.75 GHz oxygen absorption line for temperature profiling and eight additional channels near the 183.31 GHz water vapor absorption line for water vapor profiling. HAMMR was deployed on a twin otter aircraft for a west coast flight campaign (WCFC) from November 4–17, 2014. During the WCFC, HAMMR collected radiometric observations for more than 53.5 h under diverse atmospheric conditions, including clear sky, scattered and dense clouds, as well as over a variety of surface types, including coastal ocean areas, inland water and land. These measurements provide a comprehensive dataset to validate the instrument.**

***Index Terms*—Atmospheric profiling, coastal water vapor, microwave radiometry millimeter-wave radiometry.**

Manuscript received April 16, 2019; revised July 6, 2019; accepted October 9, 2019. This work was supported in part by the U.S. National Aeronautics and Space Administration, Science Mission Directorate, in part by the Earth Science Technology Office, and in part by the Instrument Incubator Program under Grants NNX11AH05G and NNX14AK70G. *(Corresponding author: Xavier Bosch-Lluis.)*

X. Bosch-Lluis was with Colorado State University Microwave Systems Laboratory, Colorado State University, Fort Collins, CO 80523 USA. He is now with the NASA/Jet Propulsion Laboratory, California Institute of Technology, Pasadena, CA 91109 USA (e-mail: javier.bosch-lluis@jpl.nasa.gov).

S. C. Reising is with Microwave Systems Laboratory, Colorado State University, Fort Collins, CO 80523 USA (e-mail: steven.reising@colostate.edu).

P. Kangaslahti, A. B. Tanner, S. T. Brown, S. Padmanabhan, C. Parashare, and O. Montes are with the NASA/Jet Propulsion Laboratory, California Institute of Technology, Pasadena, CA 91109 USA (e-mail: pekka.p.kangaslahti@jpl.nasa.gov; alan.b.tanner@jpl.nasa.gov; shannon.t.brown@jpl.nasa.gov; sharmila.padmanabhan@jpl.nasa.gov; chaitali.r.parashare@jpl.nasa.gov; oliver.montes@jpl.nasa.gov).

B. Razavi is with the Communication Circuits Laboratory, University of California Los Angeles, Los Angeles, CA 90095 USA (e-mail: razavi@ee.ucla.edu).

V. D. Hadel was with Microwave Systems Laboratory, Colorado State University, Fort Collins, CO 80523 USA. He is now with Ball Aerospace and Technologies (BATC), Boulder, CO 80021 USA (e-mail: toriehadel@gmail.com).

T. P. Johnson was with Microwave Systems Laboratory, Colorado State University, Fort Collins, CO 80523 USA. He is now with Sierra Nevada Corporation, Denver, CO 80112 USA (e-mail: thaddeus.johnso@gmail.com).

M. Ogut was with Microwave Systems Laboratory, Colorado State University, Fort Collins, CO 80523 USA. He is now with the NASA/Jet Propulsion Laboratory, California Institute of Technology, Pasadena, CA 91109 USA (e-mail: mehmet.ogut@jpl.nasa.gov).

J. Ranson is with the Earth Observing Laboratory, National Center for Atmospheric Research, Boulder, CO 80301 USA (e-mail: jranson@ucar.edu).

Color versions of one or more of the figures in this article are available online at http://ieeexplore.ieee.org.

Digital Object Identifier 10.1109/JSTARS.2019.2949590

I. Introduction

THE 2007 U.S. National Research Council (NRC)'s Earth Science Decadal Survey, entitled "Earth Science and Applications from Space: National Imperatives for the Next Decade and Beyond," [1] recommended the surface water and ocean topography (SWOT) mission as one of its Tier II Decadal Survey Missions. The NRC's midterm review in 2012, five years after the Decadal survey, entitled "Earth Science and Applications from Space: A Midterm Assessment of NASA's Implementation of the Decadal Survey," [2] pointed out that, "the Earth Science Decadal survey's Surface Water Ocean Topography (SWOT) mission is being considered as a multidisciplinary cooperative international effort that builds on a long-lived and successful U.S. and French partnership. The SWOT satellite mission will expand on previous altimetry flights (e.g., TOPEX/Poseidon) through wide-swath altimetry technology to completely cover the world's oceans and fresh water bodies with repeated high-resolution elevation measurements." [3]. The SWOT mission is currently planned to be launched in September 2021 [4].

The SWOT mission has two broad scientific objectives in oceanography and hydrology. The primary oceanographic goal is to characterize mesoscale ($\sim$5–100 km) and sub-mesoscale ($<$5 km) circulation by measuring the sea surface height at a horizontal spatial resolution of 15 km (over 68% of the world's oceans) and a vertical resolution of 1 cm (baseline) to 3 cm (threshold) [5]. Current constellations of altimeters can resolve the ocean circulation only at a coarse horizontal spatial resolution $>$200 km. However, it is necessary to obtain measurements at significantly smaller scales to understand the heat and carbon exchange between the ocean and the atmosphere as well as to improve knowledge of coastal and internal tides. The primary hydrological objective of SWOT is to improve measurement of the water cycle on a global basis. Specifically, the SWOT mission intends to measure changes in water storage of large inland bodies with surface area greater than 250 m^2 and rivers greater

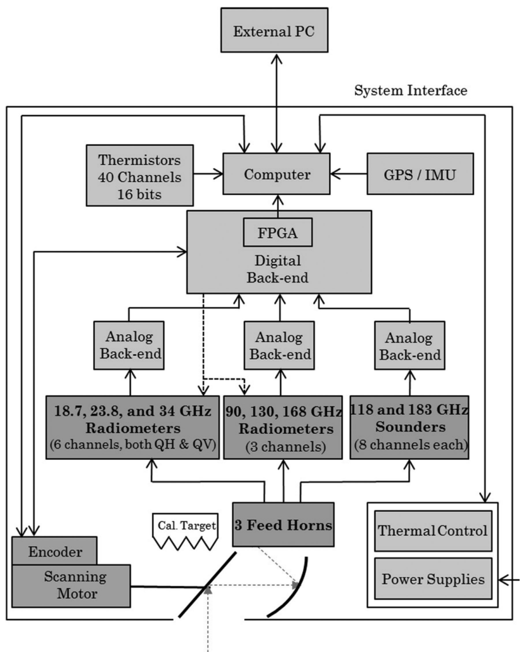

Fig. 1. HAMMR instrument block diagram indicating which participating institution is responsible for that subsystem, i.e., CSU in green, JPL in red and NCAR in blue.

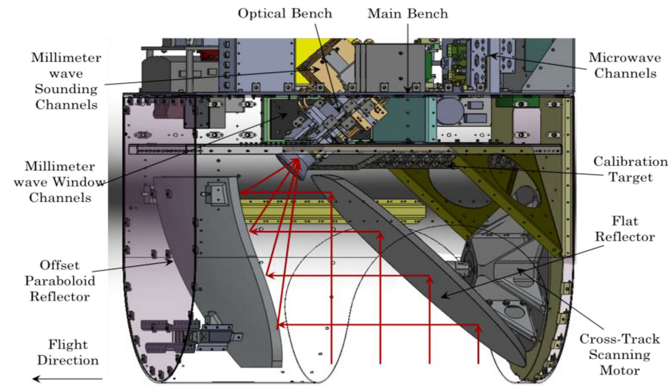

Fig. 2. HAMMR overview: CAD model showing the principal subsystems of the HAMMR instrument.

than 100 m width by measuring changes in their surface height [5]. These measurements of the global change in water storage and river dynamics are intended to improve understanding of changes in global fresh water on regional to global scales.

The high-frequency airborne microwave and millimeter-wave radiometer (HAMMR) was designed with the following primary objectives: to assess water vapor variability on 10-km and smaller spatial scales over the ocean and coastal waters; and to demonstrate high-frequency millimeter-wave radiometry using both window and sounding channels to improve coastal and overland retrievals of wet-tropospheric path delay for high-resolution ocean surface altimetry missions [6]. In addition, HAMMR was intended to be an instrument available for calibration and validation (cal/val) programs in preparation for and during the SWOT mission.

HAMMR is a cross-track scanning airborne radiometer instrument, similar in scanning configuration to HAMSR [7], with 25 channels from 18.7 to 183.3 GHz. A block diagram of the HAMMR instrument is provided in Fig. 1.

HAMMR was jointly designed and fabricated by Colorado State University (CSU), the lead institution, and the NASA/Caltech Jet Propulsion Laboratory (JPL). The University of California at Los Angeles (UCLA) designed and fabricated an application-specific integration circuit (ASIC) to serve as an analog spectrometer for the millimeter-wave temperature and humidity sounding channels. The offset paraboloidal and scanning flat reflectors were fabricated under a sub-contract from CSU to the design and fabrication services (DFS) of the Earth Observing Laboratory (EOL) of the National Center for Atmospheric Research (NCAR) in Boulder, CO, USA.

Once the construction and testing phases were completed, the HAMMR instrument was deployed on a twin otter aircraft during a west coast flight campaign (WCFC) from November 4–17, 2014, during which more than 53.5 h of data were collected. This flight campaign demonstrated the reliable operation of the HAMMR instrument from an engineering point of view, raising the system to technology readiness level 5 [8], as well as acquiring radiometric brightness temperature data to validate the utility of the HAMMR instrument for earth science measurements.

II. Instrument Description

HAMMR is a cross-track scanning airborne instrument that provides two linear-orthogonal polarization microwave measurements at 18.7, 23.8 and 34 GHz used for water vapor retrievals, similar to the advanced microwave scanning radiometer [9], millimeter-wave measurements at 90, 130, and 168 GHz used to improve spatial resolution of water vapor retrieval near coastlines, and also measurements near 118.75 GHz and near 183.31 GHz for temperature and water vapor sounding over the ocean and over land.

HAMMR is designed to fit into a small downward-looking port on an aircraft. The HAMMR instrument is housed in an aluminum structure measuring 79 cm long, 52 cm wide, and 73.5 cm tall. It has a total mass of 75 kg. A computer aided design (CAD) model of HAMMR is provided in Fig. 2.

As shown in Fig. 2, the optical subsystem consists of a rotating flat reflector for cross-track scanning and a static offset paraboloidal reflector that collimates the incoming radiation onto its focal point. The HAMMR scanning direction is perpendicular to the flight path, and its nominal scanning rate is 60 Hz. Each scan includes $\pm 45°$ of nadir scene measurements as well as observations of an ambient blackbody calibration target at zenith (with regard to the orientation shown in Fig. 2). HAMMR has three sets of radiometric receivers, each using a separate feed horn antenna. First, the low-frequency microwave Dicke-type direct-detection radiometer channels at 18.7, 23.8, and 34 GHz, based on monolithic microwave integrated circuit (MMIC) technology, perform observations at both quasi-vertical and quasi-horizontal polarizations. Second, the millimeter-wave window channels use Dicke-type direct-detection receivers at 90, 130, and 168 GHz based on 35-nm gate length InP high-electron-mobility transistor (HEMT) MMIC low-noise amplifiers (LNA) [10], [11]. Third, MMIC-based millimeter-wave spectrometers measure at eight channels just above 118.75 GHz for temperature profiling and at another eight channels just below 183.31 GHz for water vapor profiling [12]. The spectrometer is an intermediate frequency (IF) heterodyne receiver coupled with an ASIC that serves as a filter bank and down-converts each channel to baseband. Although the millimeter-wave window channels are not able to sense radiometric emission from the earth's surface under some circumstances, their frequencies are chosen to lie between the temperature absorption lines near 60 GHz and at 118.75 GHz and the water vapor absorption line at 183.31 GHz. Therefore, the term "window" is used to differentiate the 90, 130, and 168 GHz channels from the millimeter-wave sounding channels near the temperature and water vapor absorption peaks.

The command and data handling (C&DH) subsystem is based on a field programmable gate array (FPGA) that controls the data acquisition, the radiometer calibration and reads the motor position from the motor encoder. The acquisition of the radiometric channels is performed on signal conditioning printed circuit boards that integrate and digitize the output of each channel. Each measurement is time stamped and associated with a motor position. Additionally, the C&DH reads telemetry data from 40 onboard thermistors for housekeeping and radiometric calibration as well as global positioning system location and platform attitude. All of the measured data are configured and recorded by an on-board computer.

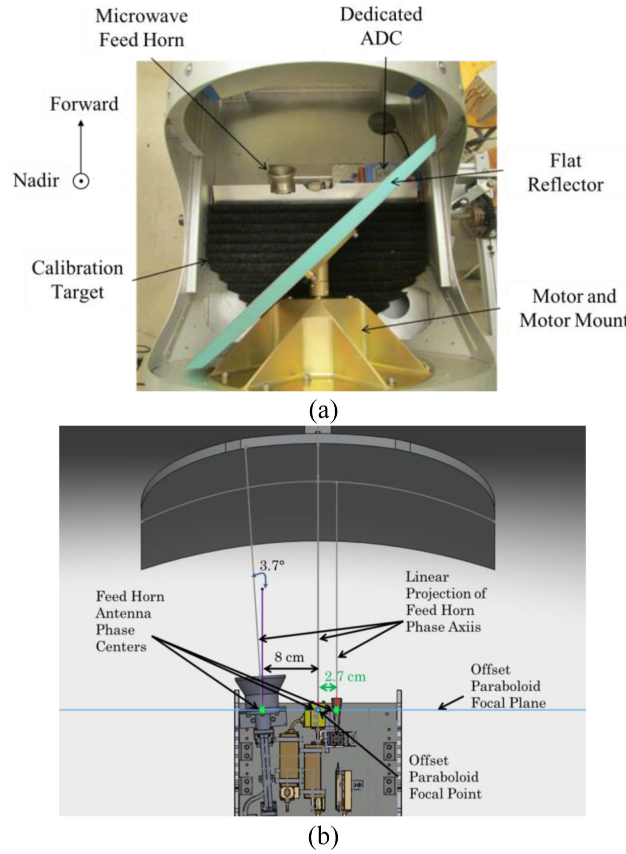

Fig. 3. Optical subsystem. (a) Configuration of ambient calibration target, flat reflector and three feed horn antennas. (b) Optical bench feed horn geometry with feed horn offsets labeled. Notice that the picture (a) and the diagram (b) have the same orientation.

A. *Optical Subsystem*

The optical subsystem consists of a flat reflector, an offset paraboloidal reflector and three feed horns, as shown in Fig. 3. The flat reflector scans the antenna beams perpendicular to the direction of flight to perform cross-track scanning. The paraboloidal reflector reflects and focuses the emission onto the three feed horns of the three sets of radiometer channels. When the flat reflector is pointed within $\pm 45°$ of nadir, the emission from the Earth scene is reflected onto the paraboloidal reflector. The flat reflector was custom designed to be lightweight and was fabricated from an aircraft aluminum honeycomb panel structure. The paraboloid reflector's front surface geometry was imported from a CAD model generated by CSU into DFS' computer-aided-manufacturing software for machining and surfacing of the reflective surface.

As shown in Fig. 3(a), the optical system includes a custom-designed, built-in blackbody target for end-to-end calibration that provides external calibration during each scan. When the flat reflector is pointed within $\pm 40°$ of zenith, the emission from the calibration target is reflected onto the paraboloidal reflector. The three feed-horn antennas are mounted in the focal plane of the paraboloidal reflector, with the feed-horn antenna for the high-frequency millimeter-wave window channels at the focal point. This feed horn was chosen to be at the focal point because it has smaller wavelength than the microwave channels and is therefore more sensitive to small displacements. The millimeter-wave window channels are the principal new technology demonstrated in the HAMMR instrument. Fig. 3(b) shows a diagram of the geometric relationships between the antennas and the paraboloidal reflector. As shown in Fig. 3(b) as viewed from earlier, the microwave feed horn is offset by 8 cm to the left, and the millimeter-wave sounding channels by 2.7 cm to the right, of the focal point of the paraboloidal reflector. Since both the microwave and millimeter-wave sounding feed-horn antennas are offset from the paraboloidal reflector's focal point, the feed-horn beams are not parallel to each other when exiting the HAMMR chassis aperture. This angular beam offset was determined theoretically and compensated in the geo-referencing algorithm. The three feed-horn antennas and the multichip modules (MCM) for the millimeter-wave window channels are mounted on a single piece of aluminum referred to as the optical bench, as shown in Fig. 4.

Since the feed horns are mounted on the optical bench, their location and orientation are fixed with respect to the chassis, ensuring the correct optical alignment of the flat reflector, paraboloidal reflector and feed horns. As a result, the entire optical assembly can be dismounted from and remounted to the rest of the HAMMR instrument for testing and debugging.

The half-power beam width (HPBW) of each of HAMMR's radiometer channels is given in Table I. As shown in Table I the 18.7 GHz microwave radiometer channel has the biggest HPBW. The footprint diameter size of 18.7 GHz channels is

This article has been accepted for inclusion in a future issue of this journal. Content is final as presented, with the exception of pagination.

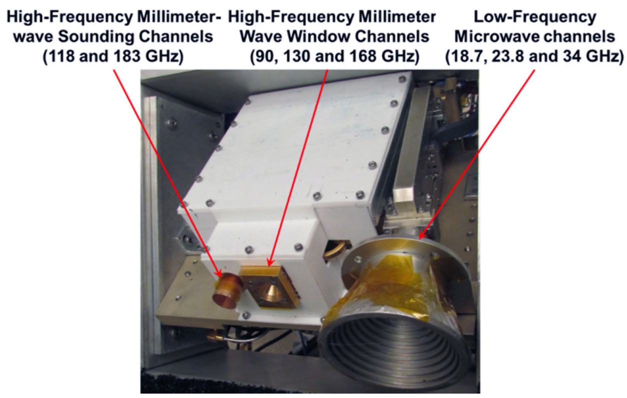

Fig. 4. Optical bench of HAMMR showing the three feed horns.

TABLE I
HALF-POWER BEAM WIDTH OF HAMMR CHANNELS

Channel Frequency (GHz)	Half-power Beam Width
18.7	3.46°
23.8	3.06°
34.0	2.14°
90.0	1.36°
130.0	0.44°
168.0	0.34°
118.8	0.95°
183.3	0.67°

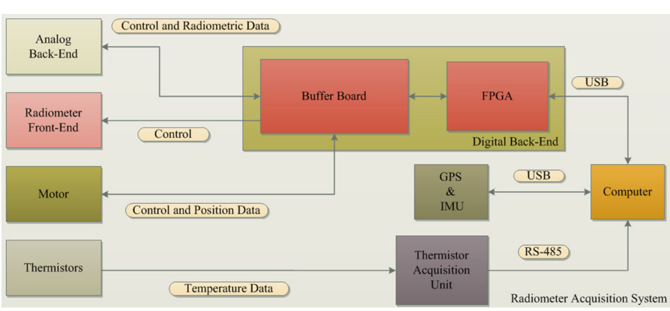

Fig. 5. Block diagram of the HAMMR C&DH subsystem.

approximately 180 m, when then instrument is deployed in nominal configuration, i.e., in an aircraft with an altitude of 3 km above ground level. On the other hand, the best HPBW is for the 168 GHz millimeter window channel, with a footprint diameter of approximately 20 m in the same conditions.

B. Command and Data Handling Subsystem

The C&DH subsystem provides signal conditioning of the radiometric channel outputs, digitizes, time stamps and associates each measurement with a motor position, and controls the Dicke and noise diode switches in the radiometer for calibration purposes. Fig. 5 shows a block diagram of the C&DH subsystem.

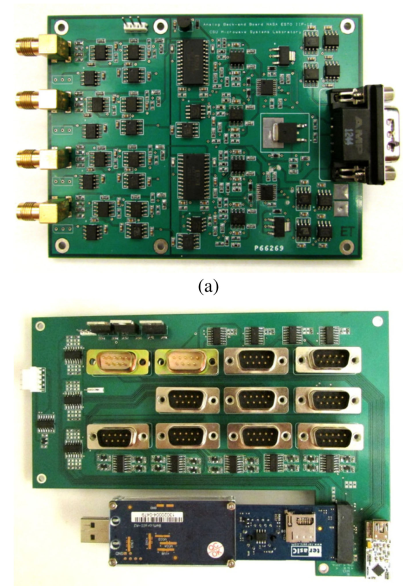

Fig. 6. C&DH subsystem views. (a) ABEB. (b) C&DH board showing the control signal connectors and the FPGA.

The core of the C&DH subsystem is an FPGA that: controls the digitization of the analog signals from the radiometers; sends and receives control signals to and from the radiometers and motor; and synchronizes the outputs of the HAMMR subsystems to be stored in the final acquisition files. Fig. 6 shows pictures of the C&DH subsystem.

The ABEBs, shown in Fig. 6(a), condition the signal, time-integrate and digitize the radiometer channel outputs using an FPGA master clock. The digitized output data are sent to the FPGA and then to an internal computer running a networked Linux operating system. Each ABEB digitizes up to four channels. The C&DH subsystem has 7 ABEBs that provide a total of 28 channels of data acquisition for the HAMMR instrument. The C&DH board, containing the FPGA, generates control signals for the radiometers, ABEBs, and motor and drives them at the appropriate voltage levels. The FPGA board is mechanically and electrically integrated with the C&DH board through a connector, as shown in Fig. 6(b). In addition, the C&DH subsystem acquires GPS location and the aircraft attitude in terms of roll, pitch and yaw using an inertial measurement unit, and records the thermistor data for housekeeping and radiometric calibration.

C. Microwave Radiometer Channels

The purpose of the microwave radiometer channels in the HAMMR instrument is to perform brightness temperature measurements at the same frequencies as the advanced microwave radiometer (AMR), currently on orbit on both OSTM/Jason-2 and Jason-3 [13]. The microwave radiometer channels are Dicke-type direct-detection radiometers, as shown in the block diagram in Fig. 7.

This article has been accepted for inclusion in a future issue of this journal. Content is final as presented, with the exception of pagination.

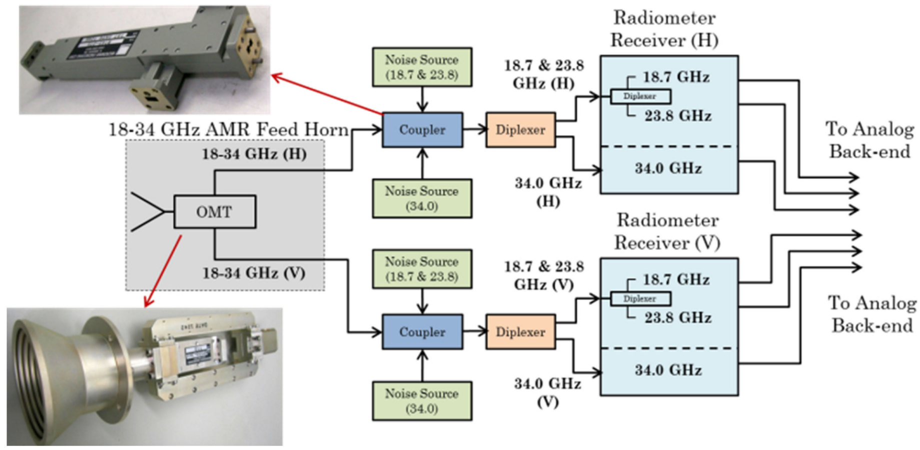

Fig. 7. HAMMR microwave radiometer block diagram.

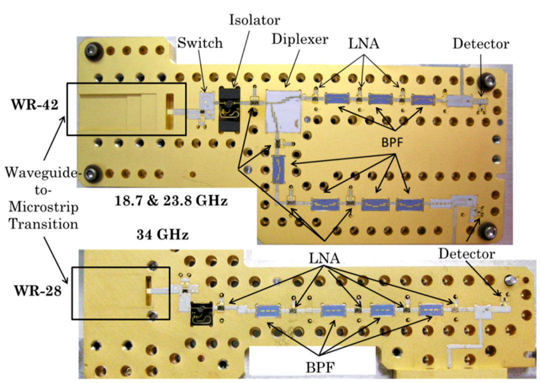

Fig. 8. HAMMR microwave radiometer receiver.

The microwave radiometer channels have center frequencies of 18.7, 23.8, and 34.0 GHz, each measuring at two orthogonal polarizations, for six microwave channels. The cross-track scanning rotates the polarization basis during the scan. The two orthogonal polarizations are referred as quasi horizontal (QH) and quasi vertical (QV) since the instrument optics do not overlap with the true H and V planes based on the scanner angle and the offset of the microwave radiometer horn antenna with respect the focal point. The microwave radiometer feed horn is followed by an orthomode transducer (OMT) to separate the QV and QH polarizations. A directional coupler couples into the receiver the outputs of two noise sources, one for 18.7 and 23.8 GHz and the other for 34.0 GHz, as shown in Fig. 7. The noise sources are used for internal calibration to determine the linear relationship between output voltage and measured antenna temperature in addition to determining the receiver noise temperature for each channel.

Fig. 8 shows the HAMMR microwave radiometer receiver. As illustrated, after the signal is converted from waveguide to microstrip, it is input to a Dicke switch. Band-pass filters (BPF) are inserted between each low noise amplifier (LNA) stage for band limiting to avoid saturation. The insertion losses of the BPFs also help to set the correct power level for the input to each detector diode.

TABLE II
PERFORMANCE OF QH POLARIZATION MICROWAVE RADIOMETER CHANNELS, AS MEASURED IN THE LABORATORY

Channel Frequency [GHz]	Receiver Noise Temperature (K) QH	Pre-Detection Bandwidth (MHz) (Theoretical) QH
18.7	550	200
23.8	570	400
34.0	620	800

The output of each detector diode is input to a video amplifier, not shown in Fig. 8, for additional amplification at baseband. The outputs of each of the microwave radiometer channels are connected to the inputs of the ABEB using coaxial cables.

Table II shows the measured receiver noise temperature and theoretical noise equivalent bandwidth for QH microwave channel measured in the laboratory using the Y-factor method. For the QV branch, the Y-factor measurement has not been measured but the receiver noise has been inferred to be similar to the QV channel, within $\pm$ 15% range. This has been estimated from the standard deviation of the subtraction of consecutive samples, to mitigate the effect of gain fluctuation, when the QV channel was looking at the external calibration target. The QV and QH channels performance difference is not relevant and might have two different sources: different front-end losses and different bandwidth due to fabrication imperfections.

D. *Millimeter-Wave Window Channels*

Initial design of the millimeter-wave window channels and the development of laboratory prototypes were completed during the ESTO-funded Advanced Component Technology 2008 (ACT-08) project at CSU and JPL [14], [15]. The frequencies of 90, 130, and 168 GHz were chosen to provide the maximum amount of information content on wet-tropospheric path delay [12]. The millimeter-wave window channels have a much larger

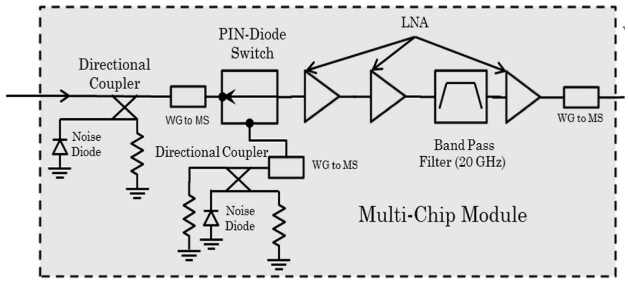

Fig. 9. Millimeter-wave window channel block diagram.

bandwidth than the microwave channels and are more sensitive to integrated water vapor. This is because the absorption, and therefore emission, of the atmosphere is much greater at millimeter-wave frequencies than at microwave frequencies. The greater absorption also makes the millimeter-wave frequencies less sensitive to surface emission [16], [17].

The millimeter-wave window channels are Dicke-type direct-detection radiometers. The block diagram of each of the millimeter-wave window channels is shown in Fig. 9.

Immediately following the trifrequency, feed horn input is a directional coupler used for internal calibration of the radiometer. The noise diode is turned on and off by changing its bias, and the corresponding noise temperatures of these two states are known values. The difference between the output powers in each of these two states is called the noise deflection. The noise deflection for each of the two noise diodes is used to verify the stability of the calibration [18]. A single-pole double-throw Dicke-type switch follows the coupler. The switch alternately connects to the input of the receiver to the antenna port, an unknown brightness temperature, and to the reference port, a known brightness temperature, to minimize gain fluctuations. The termination typically used at the reference port loads the switch differently from that at the input at the antenna port. To mitigate this imbalance, a coupler and a noise diode identical to the one at the antenna port are installed at the reference port. After the switch, the RF signal is input into an RF chain of three LNAs, where the second and third are each separated by a BPF to avoid saturation of the final LNA. The amplified signal is converted back to waveguide by a microstrip-to-waveguide transition. Directly after the MCM is a waveguide band definition filter to set the radiometer receiver's bandwidth. The filtered RF signal is directly detected by the detector diode without being down-converted.

The detector diode converts the RF signal power (input) into a baseband voltage signal (output) proportional to the input power. A video amplifier then amplifies the baseband voltage signal before being output to the ABEB, where it is digitized and integrated for data processing. Fig. 10(a) shows a photograph of the 168 GHZ module assembly and Fig. 10(b) shows the complete window millimeter wave receiver set.

Table III shows the receiver noise temperature and noise equivalent bandwidth for each millimeter-wave channel measured in the laboratory using the Y-factor method and standard gain horn antennas for each waveguide band. In addition,

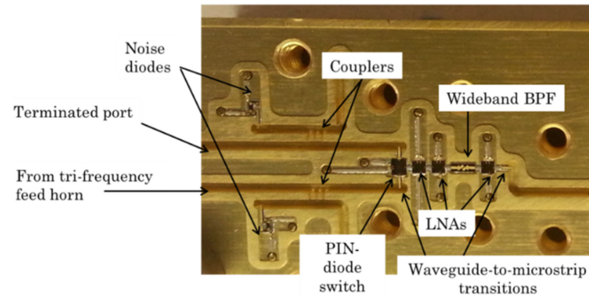

(a)

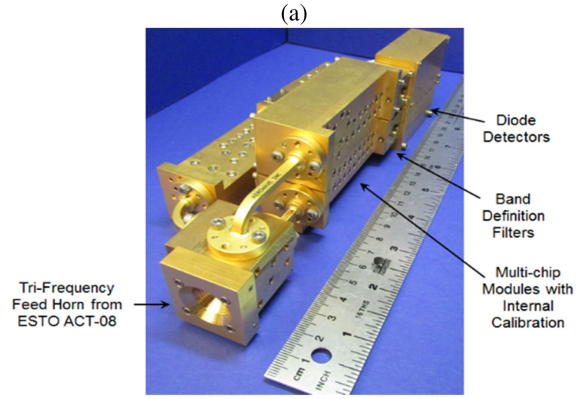

(b)

Fig. 10. Overview of the millimeter-wave window channel receivers. (a) Populated multichip module at 168 GHz. (b) Millimeter-wave window channels at 90, 130, and 168 GHz fully assembled and ready to test. Note that (b) is not the final hardware arrangement for the airborne instrument.

TABLE III
PERFORMANCE OF MILLIMETER-WAVE RADIOMETER CHANNELS, AS MEASURED IN THE LABORATORY, ALONG WITH THE OUTER DIMENSIONS AND MASS OF EACH POPULATED MULTICHIP MODULE

Channel Frequency [GHz]	Receiver Noise Temperature (K)	Pre-Detection Bandwidth (MHz) (Theoretical)
90	818	8
130	1369	12
168	2142	12

TABLE IV
MILLIMETER-WAVE RADIOMETER OUTER DIMENSIONS AND MASS OF EACH POPULATED MULTICHIP MODULE

Channel Frequency [GHz]	Length (mm)	Width (mm)	Height (mm)	Mass (g)
90	74	28	28	523
130	76	25	28	522
168	76	28	28	498

Table IV shows the outer dimensions and mass of each populated MCM.

E. Millimeter-Wave Window Channels

Unlike the microwave radiometer channels and millimeter-wave window channels, the sounding radiometers have a

This article has been accepted for inclusion in a future issue of this journal. Content is final as presented, with the exception of pagination.

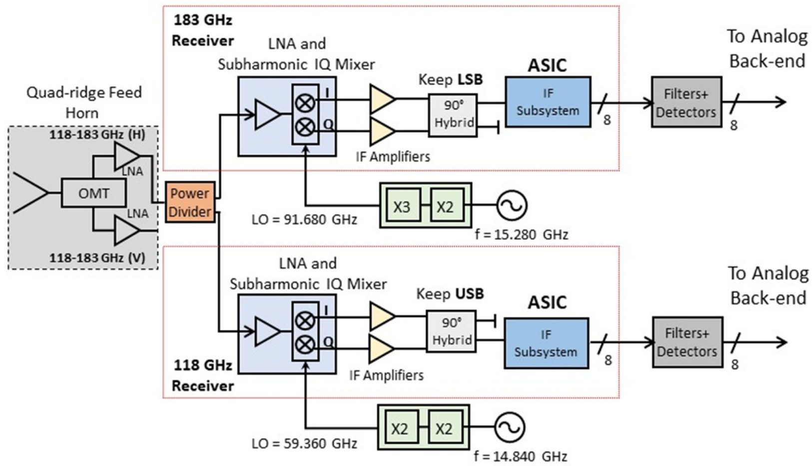

Fig. 11. Millimeter-wave sounding channel block diagram.

superheterodyne topology. The block diagram of the millimeter-wave sounders is shown in Fig. 11.

A quad-ridge feed horn, a single antenna covering the frequency range of 118 to 183 GHz, is connected to the input of the millimeter-wave sounders. The first block following the quad-ridge horn contains an OMT and two LNAs. The OMT is a polarization diplexer that divides the signal into horizontally (H) polarized and vertically (V) polarized signals. Each of the H and V signals are then amplified by an LNA.

Since only a single polarization is used for the HAMMR millimeter-wave sounders, only the H-polarization output is input to the two sounding receivers, and the V-polarization output is terminated. The output signal from the quad-ridge horn LNA is split by a waveguide diplexer into the two bands just above 118.75 GHz and just below 183.31 GHz. These two signals are input to the respective receivers for further amplification, down-conversion, and power detection. Although the 118 and 183 GHz receivers have different components that operate at their respective frequencies, their functions are identical. Once the signal enters the sounding receiver, it is input to a miniaturized housing referred to as the MMIC low mass/power radiometer (MIMRAM) [19]. The MIMRAM has two inputs: the RF input from the quad-ridge horn and the local oscillator (LO) input for the subharmonic I/Q mixer. Inside the MIMRAM are two RF LNAs and the subharmonic I/Q mixer for down-conversion. Even though the mixer produces a double sideband output, the 118 GHz receiver uses only the upper sideband (USB) and the 183 GHz receiver uses only the lower sideband (LSB).

To remove the unused sideband for each receiver, the subharmonic I/Q mixer first splits the signal into two outputs 90° out of phase with each other [20]. The I/Q outputs are output from the MIMRAM to the IF board, shown in Fig. 12.

There are two identical IF chains, one for the I signal and the other for the Q signal. Each IF chain has a low-pass filter and three IF amplifiers. At the output of the IF board, the signals travel equal lengths to a 90° hybrid coupler. The 90° hybrid coupler achieves image rejection through phase cancellation of the I and Q signals, resulting in two single sideband signals (one USB, one LSB) at the two outputs of the 90° hybrid coupler.

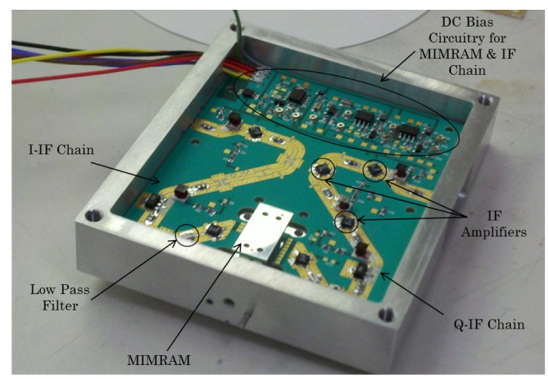

Fig. 12. Millimeter-wave sounding channel IF board.

Depending on which sideband is used, the corresponding output of the 90° hybrid coupler is input to the ASIC spectrometer. The ASIC divides the spectrum of the output signal from the hybrid coupler into eight frequency bands that are offset in increments of 1 GHz from the center frequencies of 118.75 and 183.31 GHz, as given in Table V. Three of the seven temperature profiling channels near 118.75 GHz, i.e., the low IF-frequency outputs given in Table V, are low-pass filtered directly from the hybrid coupler output instead of being input into the ASIC. Table V shows the receiver noise temperature and noise equivalent bandwidth for each millimeter-wave sounder channel measured in the laboratory using the Y-factor method and standard gain horn antennas.

III. HAMMR First Flight Campaign

Following the integration of the HAMMR instrument and extensive ground testing, initial engineering flight tests were conducted at Lake Powell, UT, USA, in July 2014. Then, a WCFC was conducted between November 4 and 17, 2014.

The primary goal of WCFC was to collect radiometric observations for atmospheric water vapor retrievals onboard Twin Otter aircraft cruising at a maximum altitude of 3 km. Fig. 13(a) shows the process of integration of the HAMMR instrument on the Twin Otter aircraft.

TABLE V
PERFORMANCE OF MILLIMETER-WAVE SOUNDING CHANNELS, AS MEASURED IN THE LABORATORY, ALONG WITH OFFSET FROM CHANNEL CENTER FREQUENCIES AND BANDWIDTH

Channel Frequency [GHz]	Receiver Noise Temperature (K)	Pre-Detection Bandwidth (GHz) (Theoretical)
118.75+0	1233	0.2
118.75+0.25	1243	0.2
118.75+0.5	1223	0.3
118.75+1	1263	0.5
118.75+2	1265	1
118.75+3	1258	1
118.75+7	1361	1
183.31-1	1553	0.5
183.31-2	1534	1
183.31-3	1580	1
183.31-4	1635	1
183.31-5	1614	1
183.31-6	1633	1
183.31-7	1622	1

(a)

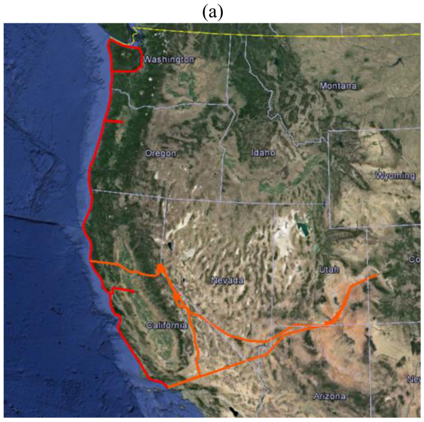

(b)

Fig. 13. WCFC overview. (a) Integration of the HAMMR instrument into the port on the Twin Otter Aircraft. (b) Flight paths during the HAMMR WCFC from November 4–17, 2014.

The HAMMR instrument operated successfully to collect more than 53.5 h of data during the WCFC under diverse atmospheric conditions, including clear sky, scattered and dense clouds, as well as a variety of surface types, including coastal ocean areas, inland water and land, as shown in Fig. 14. The WCFC began and ended at Twin Otter International, Ltd., Grand Junction, CO, USA. The flight path of the WCFC measurements is shown on Fig. 13(b).

Five flight days out of 11 were devoted to traversing nearly the entire West coast of the U.S., with overnight bases in Camarillo, CA, USA; Stockton, CA, USA; and Salem, OR, USA. HAMMR also performed radiometric measurements over inland waterways, in particular the San Joaquin River Delta (extending inland from San Francisco Bay), CA, USA, and the Strait of Juan de Fuca (leading to Puget Sound), WA, USA.

Some of the coastal and inland water areas were overflown multiple times at different times of the day to perform measurements under a variety of atmospheric conditions, including clear sky, clouds and fog. Finally, the majority of two flight days was devoted to overflights of Lake Tahoe, CA/NV, USA, and Mono Lake, CA, USA, along with the AirSWOT radar, which overflew the same two lakes on a King Air B-200, significantly higher and faster than the Twin Otter [21]. The AirSWOT radar is an airborne demonstration instrument for the KaRIn (Ka-band Radar Interferometer) for the SWOT mission.

A. Radiometric Calibration Strategy

Pre- and postflight ground calibrations were performed 18 times throughout the WCFC using a separate calibration target (external to the HAMMR instrument) consisting of a microwave absorber soaked with liquid nitrogen (LN2) (cold load) at the nadir-looking position, as well as the HAMMR built-in blackbody target for end-to-end calibration at ambient temperature (warm load) at the zenith-looking position. Ground calibrations were taken at various elevations above mean sea level and at a variety of ambient physical temperatures to determine the receiver noise temperatures of the 25 channels under different environmental conditions.

The basic radiometric calibration equation for a scanning radiometer such as HAMMR is provided in.

$$T_{\mathrm{ANT}} = G_j\left(t,\ T\right) * V_{\mathrm{ANT}} - T_{\mathrm{rec}_j}\left(T\right)[K] \qquad (1)$$

where

1) j is the jth revolution of the scanning motor.
2) $T_{\mathrm{rec}_j}(T)$ is the equivalent receiver noise temperature, and can be modeled as a function of receiver temperature based on the external pre and post flight LN2 calibration series. It is updated once per scan based on physical temperature of the receiver.
3) $G_j(t, T)$ depends not only on physical temperature but also on time, so this value is calculated from the measurements instead of from a model. This coefficient is calculated using a single point calibration, as $P_0(t) = (V_{\mathrm{ExtCal}}(t), T_{\mathrm{ExtCal}}(t))$, where $V_{\mathrm{ExtCal}}(t)$ is the internal calibration target voltage measurement for an angular range from $+5°$ to $-5°$, and $T_{\mathrm{ExtCal}}(t)$ is the spatial average of the physical temperature of the calibration target in the radiometer measured by eight thermistors distributed inside the calibration target. It is updated once per scan. Since this is an end-to-end calibration, it takes into account the antenna loses. The external calibration can be characterized as shown in (2), and after some algebraic

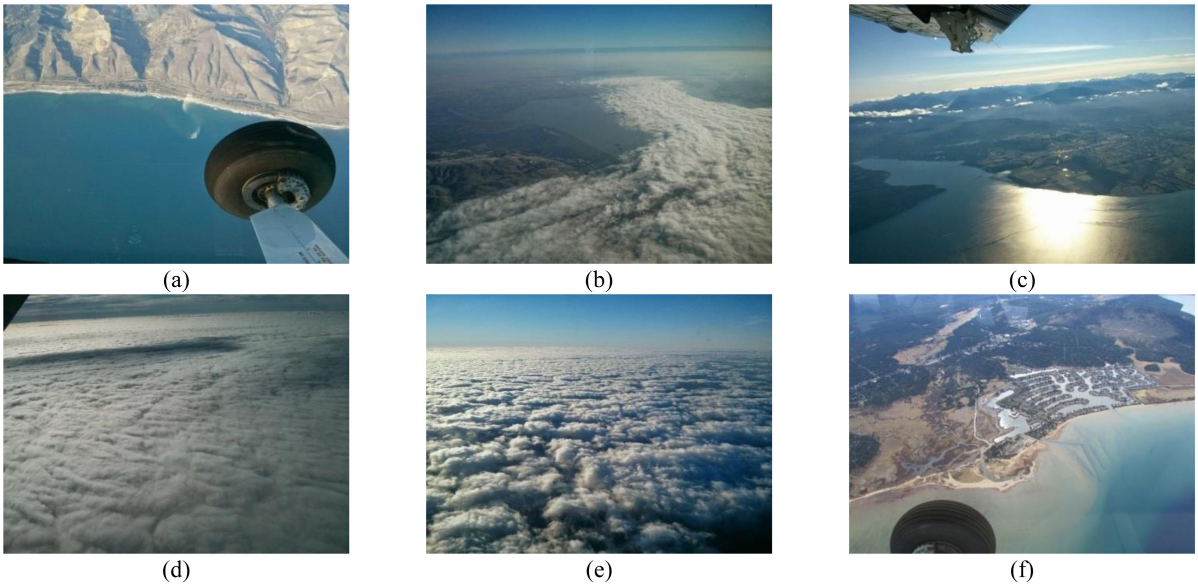

Fig. 14. Various atmospheric conditions observed during the WCFC in 2014. (a) Near Camarillo, CA, USA, November 5. (b) Near Salem, OR, USA November 7, (c) Near Port Angeles, WA, USA, November 10. (d), (e) Near Eureka, CA, November 11. (f) Over Lake Tahoe, CA/NV, USA, November 12.

manipulation, the calibration gain is determined as shown in (3)

$$T_{\mathrm{ExtCal}}(t) = G_j(t, T) * V_{\mathrm{ExtCal}}(t) - T_{\mathrm{rec}_j}(T) \quad [K] \tag{2}$$

$$G_j(t, T) = \frac{T_{\mathrm{ExtCal}}(t) + T_{\mathrm{rec}_j}(T)}{V_{\mathrm{ExtCal}}(t)} \quad [K/v]. \tag{3}$$

Both calibration coefficients, $G_j(t, T)$ and $T_{\mathrm{rec}_j}(T)$, are updated each scan based on a single point calibration from the built-in external calibration target and physical temperature of the receiver, respectively.

A $T_{\mathrm{rec}_j}(T)$ model is developed using the 18 ground calibration points dataset using the equations shown

$$G_{LN2} = \frac{(T_{amb} - T_{LN_2})}{(V_{amb} - V_{LN_2})} \quad [K/v] \tag{4}$$

$$T_{\mathrm{recLN2}} = G_{LN2} * V_{amb} - T_{amb} \; [K] \tag{5}$$

where
1) G_{LN2} is the calibration gain in Kelvin/volt.
2) T_{recLN2} is the radiometer noise equivalent temperature in Kelvin.
3) T_{LN2} is the physical temperature of the liquid nitrogen in Kelvin.
4) T_{amb} is the physical temperature of the built-in blackbody target for end-to-end calibration in Kelvin.
5) V_{amb} is the antenna voltage measured when pointing to the built-in blackbody target for end-to-end calibration. This value is averaged over an angular range of $+5°$ to $-5°$ from zenith.
6) V_{LN_2} is the antenna voltage measured when pointing to the separate LN2 external calibration target in volts, averaged over an angular range of $+5°$ to -5 from nadir.

For both, V_{amb} and V_{LN2}, averaging over the angular range considers the fact that the angular offset due to the antenna horn may is not the focal point for the microwave and sounders channels. The results of the 18 ground calibrations showed that the gain and receiver noise temperature of each of the 25 channels is linearly related to the physical temperature of the corresponding radiometer front-end, as shown in Fig. 15.

A linear best fit is used to obtain a model of the receiver noise as a function of the physical temperature of the corresponding radiometer front-end.

The small residuals of the best-fit curves obtained for all channels are given in Table VI. Residuals include both radiometer noise and errors from the calibration setup procedure when performing the calibration. The fitting lines started the assumption that the gain and receiver noise depend only on the temperature of the receiver. This was corroborated when none of the other collected parameters such as atmospheric humidity, pressure, temperature, altitude, and time of the day show any type of correlation with gain and receiver noise. Residuals are considered noise in the calibration procedure, i.e., a measurement on how confident we are on the 18 ground points collected Tcold-Thot external calibration points. As given in Table VI, low values of the residuals indicate a high degree of consistency of the recorded data and that the radiometer front-end physical temperature explains the gain and receiver noise well, indicating that the instrument is performing as expected.

The final calibration equation allows more frequent calibration, once per calibration sequence, much faster than once per second. This means that the calibration coefficients are updated every 5 ms for the millimeter-wave channels and every 123 ms for the microwave channels. There is no change for the sounders since the sounding receivers do not have a Dicke switch or the ability to inject noise at the input of the RF chain. The final calibration is obtained using (6) [22]

$$T_A = G_{\mathrm{REF}_{j,i}} * V_A(t) - T_{\mathrm{rec}_j}(T) \; [K] \tag{6}$$

where
1) j is the *j*th revolution of the scanning motor.

This article has been accepted for inclusion in a future issue of this journal. Content is final as presented, with the exception of pagination.

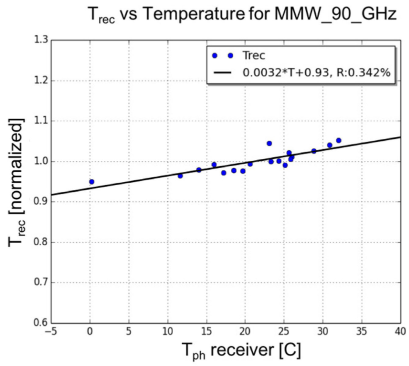

(a)

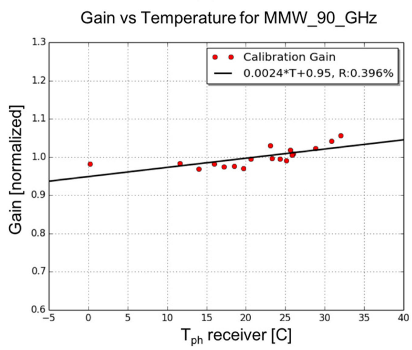

(b)

Fig. 15. Two-point ground calibration during WCFC: Linear fit for the 90 GHz channel of (a) receiver noise temperature and (b) normalized gain. Notice that the gain is only shown for comprehension, but the model is not used for the final calibration.

TABLE VI
RESIDUALS OF THE NORMALIZED CALIBRATION GAIN AND RECEIVER NOISE TEMPERATURE WITH RESPECT TO SYSTEM TEMPERATURE

Channel Frequency [GHz]	Normalized Gain Fit Residuals (%) QH | QV	Receiver Noise Fit Residuals (%) QH | QV
18.7	0.5001 | 0.4077	0.1379 | 0.1761
23.8	1.0938 | 0.4377	0.1627 | 0.2544
34.0	0.2497 | 0.7254	0.1379 | 0.1761
90	0.3956	0.6886
130	0.3419	0.4752
168	0.5671	0.5489
118.75+0	5.125	3.524
118.75+0.25	5.185	3.260
118.75+0.5	4.581	3.351
118.75+1	4.722	2.099
118.75+2	4.818	1.485
118.75+3	4.800	2.035
118.75+7	4.230	1.385
183.31-1	0.969	0.875
183.31-2	0.901	0.809
183.31-3	1.906	1.020
183.31-4	1.496	0.856
183.31-5	2.386	0.926
183.31-6	2.299	1.371
183.31-7	2.552	0.863

TABLE VII
HAMMR NEΔT MEASURED FROM THE DATA FOR INTEGRATION TIME $\tau =$ 2.78 MS FOR $\mathrm{T_{ant}} = 290$ K (CALIBRATION TARGET)

Channel Frequency [GHz]	Measured Uncertainty QV|QH [K]	Radiometer Theoretical NEΔT [K]
18.7	1.31|1.34	1.27
23.8	0.87|0.87	0.82
34.0	0.99|0.81	0.70
90	0.76	0.57
130	1.96	0.63
168	3.38	0.76
118.75+0	2.62	2.08
118.75+0.25	2.39	2.09
118.75+0.5	1.79	1.69
118.75+1	1.89	1.34
118.75+2	2.42	0.95
118.75+3	1.66	0.94
118.75+7	2.44	1.01
183.31-1	1.63	1.59
183.31-2	1.42	1.12
183.31-3	2.18	1.14
183.31-4	1.64	1.17
183.31-5	1.72	1.16
183.31-6	2.07	1.17
183.31-7	1.60	1.16

2) i is the ith calibration sequence during the jth revolution of the scanning motor.
3) $T_{\mathrm{rec}_j}(T)$ is the equivalent radiometer noise temperature, and can be modeled as a function of radiometer front-end physical temperature using the model obtained from the LN2 calibration series.
4) $G_{\mathrm{REF}_{j,i}}$ is the gain calculated using the Dicke reference, and is calculated as shown in.

$$G_{\mathrm{REF}_{j,i}} = \frac{T_{\mathrm{REF}_{\mathrm{ExtCal}_j}} + T_{\mathrm{rec}_j}(T)}{V_{\mathrm{REF}_i}}$$
$$= G_{\mathrm{ExtCal}_j}(t,\ T) * R_{\mathrm{REF}_{j,i}}\ [K/v] \quad (7)$$

where

1) $T_{\mathrm{REF}_{\mathrm{ExtCal}_j}} + T_{\mathrm{rec}_j}(T) = G_{\mathrm{ExtCal}_j}(t,T) * V_{\mathrm{REF}_{\mathrm{ExtCal}_j}}$ is the measured equivalent noise temperature when the Dicke switch is pointing to the reference load while the antenna is looking at the built-in blackbody target for end-to-end calibration during the jth revolution of the scanning motor. This value is averaged over a range of $+5°$ to $-5°$ zenith angle. This value is updated once per scan.
2) $G_{\mathrm{ExtCal}_j}(t,T)$ is the calibration coefficient calculated using the built-in blackbody target for end-to-end calibration, as shown in (4). This value is updated once per scan.
3) $V_{\mathrm{REF}_{\mathrm{ExtCal}_j}}$ is the voltage of the of the Dicke reference load when looking at the built-in blackbody target for end-to-end calibration averaged over a range of $+5°$ to $-5°$ zenith angle. This value is updated once per scan.
4) V_{REF_i} is the voltage of the of the Dicke reference load for the ith calibration sequence during the jth revolution of

This article has been accepted for inclusion in a future issue of this journal. Content is final as presented, with the exception of pagination.

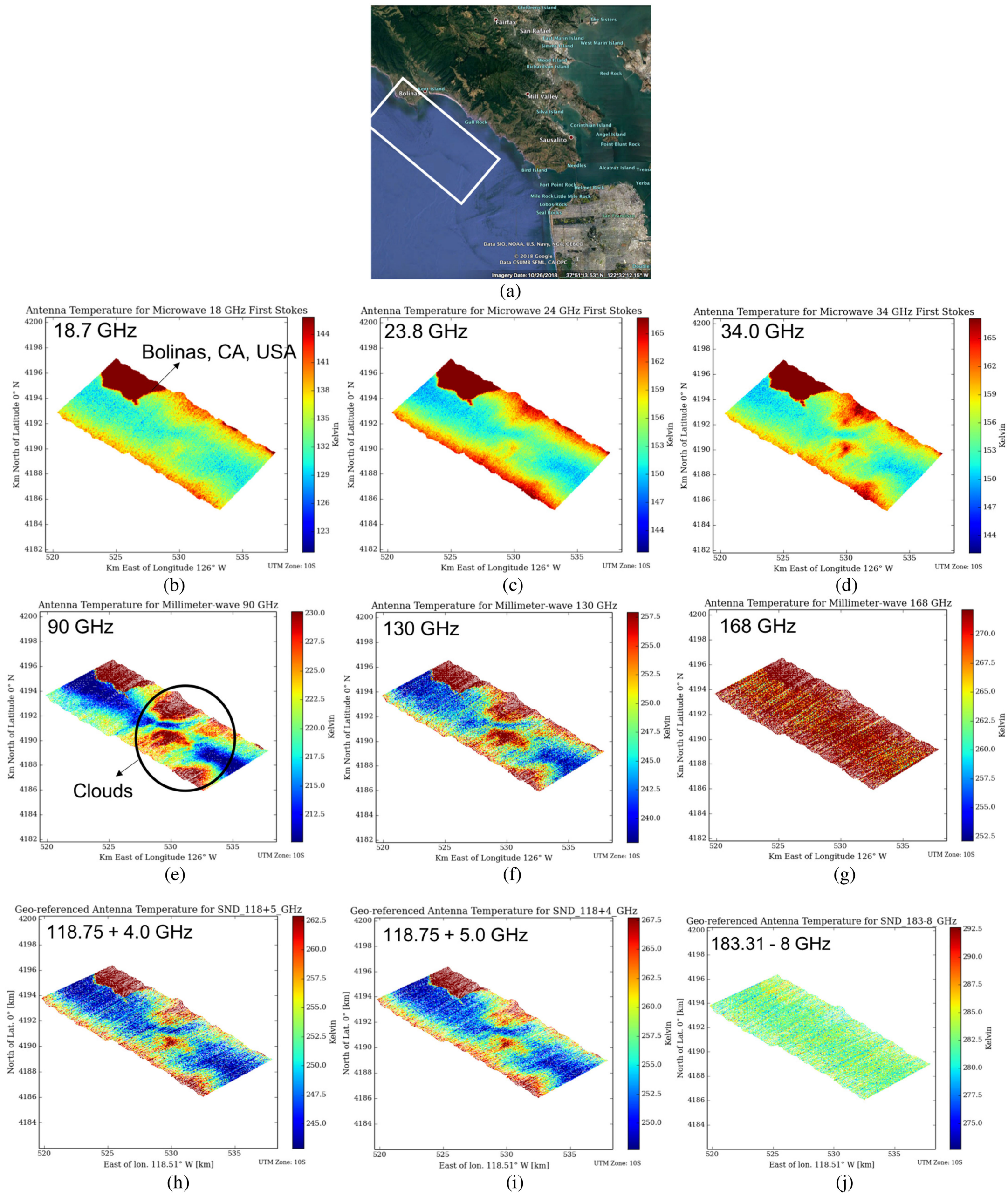

Fig. 16. Geo-referenced HAMMR-measured antenna temperatures over (a) Marin County, CA, USA. Multispectral view of the same scene. First Stokes parameters for channels (b) 18.7, (c) 23.8 and (d) 34.0 GHz channels, the millimeter-wave window (e) 90, (f) 130, and (g) 168 GHz channels, which is saturated due to the atmospheric humidity. Temperature sounder channels (h) 118.75-4 GHz and (i) 118.75 + 5 GHz. Finally a single sample for the water vapor sounder at (j) 183.31-8, which is also saturated due to water vapor content in the atmosphere.

the scanning motor. Therefore, this value is updated each calibration sequence (every 5 ms for the millimeter-wave channels and every 123 ms for the microwave channels). Furthermore, this value is averaged to reduce the measurement noise using a moving window.

5) $R_{\mathrm{REF}_{j,i}}$ is the ratio of $V_{\mathrm{REF}_{\mathrm{ExtCal}_j}}$ and V_{REF_i} i.e.,: $R_{\mathrm{REF}_{j,i}} = V_{\mathrm{REF}_{\mathrm{ExtCal}_j}} / V_{\mathrm{REF}_i}$.

B. Data-Driven Radiometric Resolution

The NEΔT is defined by ISO and the Guide to the expression of uncertainty in measurement as a type A measurement uncertainty [23]. The radiometric resolution (NEΔT) for each channel of the HAMMR instrument is given in Table VII for an integration time $\tau = 2.78$ ms and 290 K T_{ANT}. Antenna duty cycle is 50% for the microwave, 48% for the millimeter-wave window channels and 100% for the millimeter-wave sounding channels.

A comparison between the theoretical NEΔT values and the measured ones is given in Table VII. The channels showing substantial disagreement between measured and expected values are the 130 and 168 GHz window millimeter-wave channels. This was caused by the LNA 1/f noise due to a sub-optimal choice of the duration of the calibration cycle, resulting in an increase in measured NEΔT over the theoretical value of a factor of three or more.

As demonstrated afterward in [24], radiometers achieve the theoretical NEΔT when the effect of 1/f noise is minimized by switching between the antenna and the Dicke reference load at 1 kHz rate with 50% duty cycle. Furthermore, there is a disagreement between the theoretical and measured values for the millimeter-wave sounders. This is due to the fact that the down-converted signal is send to an external SMA power detector and low pass filter, then send to the ABEBs where the signal is finally video amplified, integrated and digitized. The SMA cables between the down-converter and the video amplifier allow external noise to couple in, resulting in a degradation of the NEΔT performance. This can be solved by moving the video amplifiers inside the down-converter box. These radiometric resolution (NEΔT) values do not consider spatial averaging, which is necessary and substantially reduces the noise.

C. Geo-Referenced Antenna Temperature

Fig. 16(a) shows an optical image for the measured scene to provide geographic context. The rest of the Fig. 16 shows antenna temperature multispectral information of an atmospheric state that contains clouds on November 11, 2014. The images are obtained by scanning for from $-45°$ to $+45°$ nadir defined angles. The first Stokes parameter for the microwave channels are presented [23], which accounts for any angular dependence with the measurement geometry. Channels 168 and 183.31-8 GHz are saturated due to the high water vapor content of the atmosphere.

The improved spatial resolution obtained using the millimeter-wave channels is shown in comparison to the microwave channels. Also, the level of detail in the 90 GHz image is observable due to its higher spatial resolution (nadir resolution of 25×36 m). In contrast, the 34 GHz image has blurred transitions between land and the sea, indicating a lower spatial resolution (nadir resolution of 159×224 m).

IV. Summary and Conclusion

The 25-channel, cross-track scanning HAMMR instrument was designed, built, tested and demonstrated on a Twin Otter aircraft as a collaborative effort between CSU, the lead institution, and the JPL. HAMMR consists of three sets of radiometer channels, the newly-developed high-frequency millimeter-wave window channels (90, 130, and 168 GHz), millimeter-wave sounding channels (near 118 and 183 GHz), and low-frequency microwave channels (18.7, 23.8, and 34.0 GHz), similar to the AMR instrument on OSTM/Jason-2 and Jason-3.

The HAMMR instrument was deployed on a Twin Otter aircraft during the WCFC from November 4–17, 2014. This campaign provided more than 53.5 h of observations from HAMMR under diverse atmospheric conditions, including clear sky, scattered and dense clouds, as well as a variety of surface types, including coastal ocean areas, inland water and land.

In the future, the HAMMR instrument is capable of serving a number of functions for NASA Earth Science. Deployed with AirSWOT, it could provide measurements of the wet tropospheric path delay reducing any ambiguities from the wet tropospheric correction in interpretation of the radar data, thereby improving understanding of the AirSWOT performance and the SWOT error budget. The broad frequency coverage and high spatial resolution of HAMMR also make it ideal for science-focused campaigns in the areas of weather, water and energy cycles and climate variability and change. In addition, the HAMMR instrument can provide high-spatial resolution measurements of atmospheric water vapor profile, atmospheric temperature profile, ocean surface wind speed, sea ice characterization and extent, snow water equivalent, and soil moisture over bare and lightly vegetated soils.

References

[1] National Research Council, *Earth Science and Applications from Space: National Imperatives for the Next Decade and Beyond*, Washington, DC, USA: Nat. Academies Press, 2007.

[2] National Research Council, *Earth Science and Applications from Space: A Midterm Assessment of NASA's Implementation of the Decadal Survey*, Washington, DC, USA: Nat. Academies Press, 2012.

[3] "Ocean surface topography from space," Jet Propulsion Lab., Pasadena, CA, USA. [Online]. Available: https://sealevel.jpl.nasa.gov/, Accessed on: Nov. 13, 2019.

[4] E. Lindstrom *et al.*, Summary Report of the 2nd SWOT Science Team Meeting 2017, Jun. 2017. [Online]. Available: https://swot.oceansciences.org/docs/summary_of_SWOT_2nd_Science_Team_Meeting_Toulouse_2017_27No.pdf, Accessed on: Apr. 14, 2019.

[5] E. Rodriguez and P. S. Callahan, "Surface water and ocean topography mission (SWOT) project: Science requirements document," Mar. 18. 2016. [Online]. Available: https://swot.oceansciences.org/docs/D-61923_SRD_Rev_A_20160318.pdf, Accessed on: Apr. 14, 2019.

[6] S. C. Reising *et al.*, "Development of low-mass, low-power, high-frequency microwave radiometers with internal calibration to provide high-resolution wet-tropospheric path delay measurements for the SWOT mission," in *Proc. NASA Earth Sci. Technol. Forum*, Pasadena, CA, USA, 2011.

[7] S. T. Brown *et al.*, "The high-altitude MMIC sounding radiometer for the global hawk unmanned aerial vehicle: instrument description and performance," *IEEE Trans. Geosci. Remote Sens.*, vol. 49, no. 9, pp. 3291–3301, Sep. 2011.

[8] National Aeronautics and Space Administration Earth Science Technology Office, Jul. 2014. [Online]. Available: http://esto.nasa.gov/technologists_trl.html, Accessed on: Apr. 14, 2019.

[9] D. M. Le Vine, T. T. Wilheit, R. E. Murphy, and C. T. Swift, "A multifrequency microwave radiometer of the future," *IEEE Trans. Geosci. Remote Sens.*, vol. 27, no. 2, pp. 193–199, Mar. 1989.

[10] P. Kangaslahti *et al.*, "Sub-20-K noise temperature LNA for 67–90 GHz frequency band," in *Proc. 2017 IEEE MTT-S Int. Microw. Symp. Dig.*, Jun. 4–9. 2017.

[11] S. C. Reising *et al.*, "InP HEMT low-noise amplifier-based millimeter-wave radiometers from 90 to 180 GHz with internal calibration for remote sensing of atmospheric wet-path delay," in *Proc. IEEE/MTT-S Int. Microw. Symp. Dig.*, Montreal, QC, Canada, Jun. 2012.

[12] S. Sahoo, X. Bosch-Lluis, S. C. Reising, and J. Vivekanandan, "Radiometric information content for water vapor and temperature profiling in clear skies between 10 and 200 GHz," *IEEE J. Sel. Topics App. Earth Observ. Remote Sens.*, vol. 8, no. 2, pp. 859–871, Feb. 2015.

[13] F. Maiwald *et al.*, "Reliable and stable radiometers for jason-3," *IEEE J. Sel. Topics Appl. Earth Observations Remote Sens.*, vol. 9, no. 6, pp. 2754–2762, Jun. 2016.

[14] D. Albers, "Design, fabrication, and demonstration of low-mass, low-power, small-volume, direct detection millimeter-wave radiometers at 92 and 130 GHz," M.S. Thesis, Colorado State Univ., Fort Collins, CO USA, 2012.

[15] A. Lee, "Developoment and fabrication of internally-calibrated, MMIC-based millimeter-wave radiometers at 92 GHz and 166 GHz," M.S. Thesis, Colorado State Univ., Fort Collins, CO USA, 2012.

[16] P. W. Rosenkranz, "Water vapor microwave continuum absorption: A comparison of measurements and models," *Radio Sci.*, vol. 33, no. 4, pp. 919–928, Jul. 1998.

[17] P. W. Rosenkranz, "Erratum: 'Water vapor microwave continuum absorption: A comparison of measurements and models," *Radio Sci.*, vol. 34, no. 4, p. 1025, 1999.

[18] M. A. Janssen, *Atmospheric Remote Sensing by Microwave Radiometry*, New York, NY, USA, Wiley, 1993.

[19] P. Kangaslahti, A. Tanner, B. Lambrigsten, and D. Pukala, "MIMRAM — miniature MMIC low mass/power radiometers for geostationary thinned aperture radiometer," in *Proc. NASA Earth Sci. Technol. Conf.*, College Park, MD, USA, 2007.

[20] F. Ulaby, R. Moore, and A. Fung, *Microwave Remote Sensing: Active and Passive, Vol. I - Microwave Remote Sensing Fundamentals and Radiometry, Reading*, Reading MA, USA: Addison-Wesley, 1981.

[21] L. H. Pitcher *et al.*, "First AirSWOT interferometric radar water surface elevations and flooded inundation extent from the sacramento river and edwards AFB wetland complex, California," in *Proc. AGU Fall Meeting Abstracts*, Dec. 2014.

[22] W. J. Wilson, A. B. Tanner, F. A. Pellerano, and K. A. Horgan, "Ultra stable microwave radiometers for future sea surface salinity missions appendix 4 - Running average delta-T optimization," Apr. 2005. [Online]. Available: https://trs.jpl.nasa.gov/bitstream/handle/2014/40833/D-31794_A.pdf, Accessed on: Apr. 14, 2019.

[23] J. Randa *et al.*, "Recommended Terminology for Microwave Radiometry," Nat. Inst. Std. Technol., Gaithersburg, MD, USA, 2008.

[24] J. Kloosterman *et al.*, "The advanced microwave radiometer-climate quality (AMR-C) instrument for sentinel-6," in *Proc. 28th Int. Symp. Space Terahertz Technol.*, Cologne, Germany, Mar. 13–17. 2017.

Xavier Bosch-Lluis (SM'xx) received the B.S and M.S degrees in telecommunications engineering from the Universitat Politecnica de Catalunya, Barcelona, Spain, where he received the Ph.D. degree in remote sensing from the Department of Signal Theory and Communications.

He was a Post-doc with the Department of Electrical and Computer Engineering, Microwave Systems Laboratory, Colorado State University, Fort Collins, CO, USA. At the MSL, he was with the High-Frequency Airborne Microwave and Millimeter-wave Radiometer instrument to demonstrate increased spatial resolution of wet-tropospheric path delay retrieval for high-resolution ocean surface altimeter missions. He also with the Tropospheric Water and Cloud Ice instrument, designed for operation in a 6U CubeSat, with the scientific goal of providing global measurements of upper tropospheric water vapor as well as cloud ice particle size distribution and total cloud ice water content variability. He is currently a Technologist with the Microwave Systems Technology Group Jet Propulsion Laboratory, California Institute of Technology, Pasadena, CA, USA. His research interests include microwave and millimeter-wave radiometer design and calibration, as well as innovative digital radiometric concepts such as digital beamforming or polarization synthesis.

Steven C. Reising (S'88–M '98–SM '04) received the B.S.E.E. (magna cum laude) and M.S.E.E. degrees in electrical engineering from Washington University in St. Louis, Saint Louis, MO, USA, and the Ph.D. degree in electrical engineering from Stanford University, Stanford, CA, USA, in 1998.

Since July 2011, he has been a Full Professor in electrical and computer engineering with Colorado State University, Fort Collins, CO, USA, where he was an Associate Professor from 2004 to 2011. Before joining the CSU Faculty in 2004, he was an Assistant Professor in electrical and computer engineering with the University of Massachusetts Amherst, Amherst, MA, USA, from 1998 to 2004, where he received tenure. He was a Summer Faculty Fellow for three years in the Remote Sensing Division, Naval Research Laboratory, Washington, DC, USA. For the first six months of 2014, he was a Visiting Faculty Member of the Sorbonne Universities, University of Paris VI, Université Pierre et Marie Curie, Paris, France. He has been the Principal Investigator of 14 Grants from NASA, National Science Foundation (NSF), Department of Defense, Office of Naval Research, Naval Research Laboratory, National Polar-orbiting Operational Environmental Satellite System Integrated Program Office, European Space Agency and Ball Aerospace and Technologies Corporation. He has served as Principal Faculty Advisor for 17 M.S./Ph.D. students who have completed their degrees and are now employed in universities, industry and government laboratories in the U.S., Europe and Asia. His research interests span a broad range of remote sensing disciplines, including microwave remote sensing of the Earth's atmosphere and oceans from airborne platforms, small satellites and CubeSats; radiometer systems from microwave to sub-millimeter-wave and THz frequencies (18-850 GHz); low-noise monolithic microwave integrated circuit design and packaging; lidar systems for sensing temperature and winds in the middle and upper atmosphere; lighting-ionosphere interactions and atmospheric electrodynamics.

Dr. Reising was the recipient of the 2015 George T. Abell Outstanding Research Faculty Award from the College of Engineering at Colorado State University. In 2016, he was the recipient of the Outstanding Service Award from the U.S. National Committee of the International Union of Radio Science (USNC-URSI), presented at the Plenary Session of the 2016 National Radio Science Meeting in Boulder, CO, USA. He was also the recipient of the NSF CAREER Award (2003–2008) in the areas of physical and mesoscale dynamic meteorology, and the Office of Naval Research Young Investigator Program (YIP) Award (2000–2003) for passive microwave remote sensing of the oceans. His Ph.D. student Sharmila Padmanabhan was recipient of the Second Prize Student Paper Award at IGARSS 2003 in Toulouse, France, as well as the URSI Young Scientist Award at the General Assembly in New Delhi, India, in 2005. He won the URSI Young Scientist Award at the General Assembly in Toronto, Canada, in 1999. While at Stanford, he received First Place in the USNC-URSI Student Paper Competition at the 1998 National Radio Science Meeting in Boulder, Colorado. He is the Chair of the Ad-hoc Committee for Intersocietal Relations and as an elected Administrative Committee (AdCom) Member (2003–present) of the IEEE Geoscience and Remote Sensing Society (GRSS). He currently serves as the Vice-Chair of Operations, a member of the Personnel Management Committee and as an elected AdCom Member (2014–present) of the IEEE Microwave Theory and Techniques Society (MTT-S). He previously served as the IEEE MTT-S Inter-Society Committee Chair (2015–2018), IEEE GRSS Vice President of Information Resources (2011–2018), the IEEE GRSS as the Vice President of Technical Activities (2008–2010), an Editor of the GRSS Newsletter (2000–2002) and an Associate Editor for University Profiles (1998–2000). He was a Founding Member of the Editorial Board of the IEEE GEOSCIENCE AND REMOTE SENSING LETTERS (GRSL), with an Impact Factor of 2.9 in 2017, and was an Associate Editor from 2004 to 2013. He has been a Guest Editor of three Special Issues and one Special Section of the IEEE TRANSACTIONS ON GEOSCIENCE AND REMOTE SENSING (TGRS), with an Impact Factor of 4.7 in 2017. He was the U.S. National Committee of the International Union of Radio Science (USNC-URSI) as Immediate Past Chair (2015–2017), the Chair (2012–2014) and a Secretary (2009–2011) of all ten URSI Commissions (ten scientific and technical areas). He was a Secretary of USNC-URSI Commission F (Wave Propagation and Remote Sensing) from 2004 to 2007. He founded and chaired the first three URSI International Student Paper Prize Competitions at the URSI General Assemblies and Scientific Symposia held in Chicago, IL, USA in 2008; Istanbul, Turkey, in 2011; and Beijing, China, in 2014. Prior to that, he chaired the USNC-URSI Student Paper Prize Competition from 2004 to 2008 and at the URSI North American Radio Science Meeting in Ottawa in 2007. In addition, he was a Technical Program Co-Chair for the USNC-URSI National Radio Science Meetings held each January in Boulder, Colorado, from 2010 to 2014. He is a member of URSI Commissions F, G, and H, the American Meteorological Society, the American Geophysical Union, the American Association for the Advancement of Science, Tau Beta Pi and Eta Kappa Nu.

Pekka Kangaslahti (S'94–M'98) received the M.Sc. and Ph.D. degrees from Aalto University (formerly the Helsinki University of Technology), Espoo, Finland, in 1992 and 1999, respectively.

He is a currently Group Supervisor and a Principal Engineer with the Microwave Systems Technology Group, Jet Propulsion Laboratory, California Institute of Technology, Pasadena, CA, USA. His research interests include development of millimeter-wave and submillimeter-wave monolithic microwave integrated circuits, modules, receivers and receiver arrays.

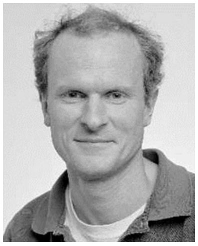

Alan B. Tanner is a Principal Engineer with NASA's Jet Propulsion Laboratory, where he has been employed since 1989. He specializes in the design and calibration of microwave radiometers and scatterometers for remote sensing of the earth. Alan has been the Lead System Engineer for the Geostationary Synthetic Thinned Array Radiometer (GeoSTAR), the Ultra-Stable Radiometer testbed (which formed the basis of the Aquarius and Juno radiometer designs), the Advanced Water Vapor Radiometers for the Cassini Gravitational Wave Experiment, the Airborne Cloud Radar (a 94 GHz scatterometer which preceded the CloudSat mission), and the Airborne Rain Mapping Radar (for Tropical Rainfall Measurement Mission). For his graduate work at the University of Massachusetts Microwave Remote Sensing Lab, he developed the Electronically Scanned Thinned Array Radiometer for soil moisture measurements, and the Stepped Frequency Microwave Radiometer for hurricane wind speed detection.

Shannon T. Brown received the B.S degree in meteorology from Pennsylvania State University, State College, PA, USA, and the M.S. degree in Atmospheric Science from the University of Michigan, Ann Arbor, MI, USA, where he also received the Ph.D. degree in geoscience and remote sensing.

He is a Principal Technologist with the NASA Jet Propulsion Laboratory in Pasadena, CA, USA. He was with JPL in 2005 as a member with the microwave advanced systems section. He has been involved with the spaceborne Topex, Jason-1, 2 and 3 Microwave Radiometers and the WindSat Polarimetric Radiometer. He is currently the Principal Investigator of the Compact Ocean Wind Vector Radiometer being developed for the US Air Force and Instrument Scientist for the NASA Juno Microwave Radiometer on the Juno New Frontiers mission to Jupiter. He is a member of the Ocean Surface Topography Science Team, the Ocean Salinity Science Team, the SMAP Science Team and the Juno Science Team. His research interests include microwave radiometer system development, calibration, geophysical algorithm development for both passive and active sensors, extraction of climate data records and radiometer science.

Dr. Brown was the recipient of NASA Exceptional Achievement Medal in 2009 and the JPL Lew Allen Award in 2010. He was also the recipient of eight NASA Group Achievement Awards and a NASA Space Act award in 2012.

Sharmila Padmanabhan received the Ph.D. degree from Colorado State University, Fort Collins, CO, USA, in 2009.

She is currently a Section Staff member with the Instrument Electronics and Software Section, Jet Propulsion Laboratory, California Institute of Technology, Pasadena, CA, USA. Her research interests include millimeter, submillimeter-wave and infrared instrumentation for remote sensing, calibration/validation and performance assessment of microwave radiometers, and geophysical retrieval algorithm development.

Chaitali Parashare received the B.E. degree in instrumentation and control from the Government College of Engineering, Pune, India in 2002, the M.S. degree in radio astronomy and space science from the Chalmers University of Technology, Göteborg, Sweden in 2004, and the Ph.D. degree in electrical engineering from the University of Virginia, Charlottesville, VA, USA in 2011.

From 2011 to 2013, she was a Postdoctoral Scholar with the NASA's Jet Propulsion Laboratory, California Institute of Technology, Pasadena, CA, USA, where she worked on internally-calibrated millimeter-wave radiometers to improve the wet-tropospheric path delay correction accuracy in coastal regions. Since 2013, she has been a member of the Radar Science and Engineering section of the NASA's Jet Propulsion Laboratory, California Institute of Technology, Pasadena, CA, USA, where she has been involved in various radar projects including RainCube—a rain-profiling and the first radar in a CubeSat, VIPR—a tunable G-band radar designed for humidity and cloud remote sensing from an airborne platform, and REASON—a dual-frequency, ice penetrating radar on the Europa Clipper mission to Jupiter's moon Europa.

Oliver Montes received the B.S. and M.S. degrees in electrical engineering from the University of California, Los Angeles, CA, USA, in 2007 and 2010, respectively.

In 2007, he was the Microwave Systems Technology Group, JPL, where he has worked on MMIC design of low-noise amplifiers and microwave switches, as well as multiple radiometer instruments for both space and airborne missions. Some of the microwave radiometers he has worked on include the HAMMR 118/183 GHz Sounder, JUNO Microwave Radiometer, Jason-3 Advanced Microwave Radiometer, Sentinel-6 High Resolution Microwave Radiometer, and the Compact Ocean Wind Vector Radiometer. He has also worked on the SHERLOC Deep-UV spectrometer and PIXL X-ray spectrometer instruments for the Mars2020 Rover. He is working on the Multi-Angle Imager for Aerosols (MAIA) instrument as the Lead Electronics Systems Engineer.

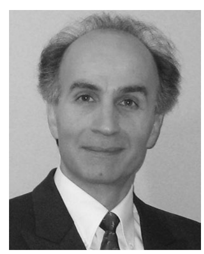

Behzad Razavi received the BSEE degree from the Sharif University of Technology, Tehran, Iran, in 1985, and the MSEE and PhDEE degrees from Stanford University, Stanford, CA, USA, in 1988 and 1992, respectively.

He was with AT&T Bell Laboratories and Hewlett-Packard Laboratories until 1996. Since 1996, he has been an Associate Professor and subsequently a Professor in electrical engineering with the University of California, Los Angeles, CA, USA. He was an Adjunct Professor with Princeton University from 1992 to 1994, and with Stanford University in 1995. He is the author of *Principles of Data Conversion System Design* (IEEE Press, 1995), *RF Microelectronics* (Prentice Hall, 1998, 2012) (translated to Chinese, Japanese, and Korean), *Design of Analog CMOS Integrated Circuits* (McGraw-Hill, 2001, 2016) (translated to Chinese, Japanese, and Korean), *Design of Integrated Circuits for Optical Communications* (McGraw-Hill, 2003, Wiley, 2012), *Design of CMOS Phase-Locked Loops* (Cambridge University Press, 2020), and *Fundamentals of Microelectronics* (Wiley, 2006) (translated to Korean, Portuguese, and Turkish), and the Editor of *Monolithic Phase-Locked Loops and Clock Recovery Circuits* (IEEE Press, 1996), and *Phase-Locking in High-Performance Systems* (IEEE Press, 2003). His current research includes wireless and wireline transceivers and data converters.

Prof. Razavi was on the Technical Program Committees of the International Solid-State Circuits Conference (ISSCC) from 1993 to 2002 and VLSI Circuits Symposium from 1998 to 2002. He was also the Guest Editor and an Associate Editor for the IEEE JOURNAL OF SOLID-STATE CIRCUITS, IEEE TRANSACTIONS ON CIRCUITS AND SYSTEMS, and *International Journal of High Speed Electronics*. He is currently the Editor-in-Chief for the IEEE SOLID-STATE CIRCUITS LETTERS. He was the recipient of the Beatrice Winner Award for Editorial Excellence at the 1994 ISSCC, the Best Paper Award at the 1994 European Solid-State Circuits Conference, the Best Panel Award at the 1995 and 1997 ISSCC, the TRW Innovative Teaching Award in 1997, the Best Paper Award at the IEEE Custom Integrated Circuits Conference in 1998, the McGraw-Hill First Edition of the Year Award in 2001, the 2012 Donald Pederson Award in Solid-State Circuits, and the American Society for Engineering Education PSW Teaching Award in 2014, the 2017 IEEE CAS John Choma Education Award. He was the co-recipient of both the Jack Kilby Outstanding Student Paper Award and the Beatrice Winner Award for Editorial Excellence at the 2001 ISSCC. He was also the recipient of the Lockheed Martin Excellence in Teaching Award in 2006, the UCLA Faculty Senate Teaching Award in 2007, and the CICC Best Invited Paper Award in 2009 and in 2012. He was the co-recipient of the 2012 and the 2015 VLSI Circuits Symposium Best Student Paper Awards and the 2013 CICC Best Paper Award. He was also recognized as one of the top 10 authors in the 50-year history of ISSCC. He is a member of the US National Academy of Engineering. He has served as an IEEE Distinguished Lecturer.

Victoria D. Hadel received the B.S. and M.S. degrees in electrical engineering from Colorado State University, Fort Collins, CO, USA.

During her research for her Master of Science degree at the Microwave Systems Laboratory, she contributed to the development of the High-Frequency Airborne Microwave and Millimeter-wave Radiometer (HAMMR), which demonstrated increased spatial resolution of wet-tropospheric path delay retrieval for high-resolution ocean surface altimeter missions. She is currently a Microwave Engineer with Ball Aerospace and Technologies, Boulder, CO, USA, where her expertise is in high-frequency, low-observable antenna design.

Thaddeus P. Johnson attended for both the B.S. and M.S. degrees in electrical engineering with Colorado State University, Fort Collins, CO, USA.

He was with the CSU Microwave Systems Laboratory on the high-frequency airborne microwave and millimeter-wave radiometer instrument focusing on system design, calibration, and verification. He is currently with Sierra Nevada Corporation, Denver, CO, USA, as an Electrical Engineer. His work has focused primarily on radio frequency circuit design and system integration.

Mehmet Ogut received the B.S. degree in electrical and electronics engineering from Bogazici University, Istanbul, Turkey in 2011, the M.S degree in electrical engineering from George Washington University, Washington, DC, USA, in 2013, and the Ph.D. degree in electrical engineering from Colorado State University (CSU), Fort Collins, CO, USA, in 2018.

During the Ph.D. study, he was with the Tropospheric Water and Cloud Ice (TWICE) small satellite instrument at the Microwave Systems Laboratory (MSL) of CSU, as a Graduate Research Assistant. TWICE is a NASA Earth Science Technology Office (ESTO) Instrument Incubator Program (IIP-13) award to develop a millimeter- and sub-millimeter-wave (118 GHz to 670 GHz) radiometer instrument including both window and sounding channels for 6U CubeSat deployment. He focused on the design and testing command and data handling, and power regulation boards, on-orbit reliability analysis of the TWICE instrument including radiation testing and analysis of electrical components, and testing, characterization and calibration of TWICE receivers. In addition, he worked on the deep-learning techniques on the microwave and millimeter-wave radiometry. He applied the deep-learning calibration to High-Frequency Airborne Microwave and Millimeter-wave Radiometer NASA ESTO IIP-10 project instrument. He is currently a Post-doctoral Research Fellow with the Microwave Instrument Science Group at the Jet Propulsion Laboratory, California Institute of Technology, Pasadena, CA, USA. His research interests include design, testing, calibration and analysis of microwave and millimeter-wave radiometer instruments, developing innovative concepts in radiometry and artificial intelligence applications in remote sensing.

Dr. Ogut is a member of Eta Kappa Nu, IEEE GRSS and MTTS societies. He was the IEEE R5 ExCom Member (2018-2019) and the Chair of IEEE High Plains Section Young Professionals Affinity Group (2017–2018).

James A. Ranson received the B.Sc. degree in mechanical engineering from the University of Colorado at Denver, Co, USA.

He is the Technical Manager of the Design and Fabrication Services (DFS) for NCAR's Earth Observing Laboratory. He was with the NCAR's Earth Observing Laboratory in 2011 and his responsibilities include the operations of the DFS facility and the technical management of the DFS mechanical engineers, technicians, and instrument makers. This facility supports NCAR and the broader atmospheric sciences community with instrument development and manufacturing. Since his arrival at the National Center for Atmospheric Research (NCAR), he has been recognized with the UCAR Scientific and Technical Advancement Award in 2014 for his contributions on the NCAR Sunrise II Gondola System and with the UCAR Scientific and Technical Advancement Award for his contributions on the Micro-pulse DIAL development in 2018. Prior to joining NCAR, he was a Principal Engineer for Lockheed Martin Coherent Technologies where he was recognized with both the Lockheed Martin Exceptional Service Award and Lockheed Martin Team Excellence Award in 2007. He is a member of the American Society of Mechanical Engineers. His research interests include instrument and sensor development, optomechanical engineering, LIDAR systems development, precision mechanics, thermal and mechanical systems engineering, electronics packaging, and advanced manufacturing for the development of instruments used on air-borne, space-borne, mobile, and ground based platforms.